ORIGINAL ARTICLE

Single-route synthesis of binary metal oxide loaded coconut shell and watermelon rind biochar: Characterizations and cyclic voltammetry analysis

Nurizan Omar[1] · Ezzat Chan Abdullah[1] · Ashley Aaron Petrus[1] · Nabisab Mujawar Mubarak[2] · Mohammad Khalid[3] · Elochukwu Stephen Agudosi[1] · Arshid Numan[3,4] · Siti Rahmah Aid[1,5]

Abstract
Generally, the type of biomass precursors is one of the key factors affecting the properties of synthesized biochar. This novel study therefore examined the single-route preparation of coconut shell and watermelon rind biochar with the combination of two types of binary metal oxide, iron nickel oxide (Fe_2NiO_4), and cobalt iron oxide ($CoFe_2O_4$) by employing a novel vacuum condition in an electric muffle furnace. The samples were characterized by several methods such as Fourier transform infrared (FTIR), field emission scanning electron microscope (FESEM), thermogravimetric analysis (TGA), X-ray diffraction (XRD), and Brunauer–Emmett–Teller (BET) Surface Area. The optimum pyrolysis temperature for producing a high surface area of 322.142 m^2/g and 441.021 m^2/g for coconut shell biochar and watermelon rind biochar, respectively, was recorded at 600 °C. FTIR analysis revealed lesser adsorption bands found in FTIR spectrum of the samples with higher pyrolysis temperature (500–700 °C). In addition, FESEM results also revealed the surface changes of the samples with the impregnation of $CoFe_2O_4^4$ and Fe_2NiO_4. Furthermore, the value added application of biochar in electrochemical energy storage has been explored in the present work. In typical three-electrode configuration, WR-BMO 600 exhibits about 152.09 Fg^{-1} with energy density about 19.01 Wh kg^{-1}.

Keywords Biochar · Binary metal oxide · Coconut shell · Watermelon rind · Pyrolysis

1 Introduction

The emerging of electronics has rapidly increased the demand for energy storage devices. On the other hand, the aggravation of environmental pollution and the depletion of fossil fuels have stimulated the development of green, renewable, and favorable energy storage devices [1–3]. Supercapacitors, batteries, fuel cells, and conventional capacitors are renowned typical smart energy technologies. Among all, supercapacitors have drawn intensive attention because of its rapid charge-discharge rate, high power density, long cycle life, and eco-friendliness [4]. However, supercapacitors have low energy density which limit their practical applications [2].

To date, numerous investigations have focused on the development of green and low cost materials aimed for good electrochemical performance. Various types of carbon materials, such as carbon nanotubes, graphene, activated carbon, and carbon aerogels have been explored as promising candidates for supercapacitor materials due to their high electrical conductivity and large specific surface area. Biochar is a carbonaceous material which possesses many excellent

✉ Ezzat Chan Abdullah
  ezzatc@utm.my

✉ Nabisab Mujawar Mubarak
  mubarak.mujawar@curtin.edu.my; mubarak.yaseen@gmail.com

✉ Mohammad Khalid
  khalids@sunway.edu.my

1 Malaysia–Japan International Institute of Technology (MJIIT), Universiti Teknologi Malaysia (UTM), Jalan Sultan Yahya Petra, 54100 Kuala Lumpur, Malaysia

2 Department of Chemical Engineering, Faculty of Engineering and Science, Curtin University, 98009 Miri, Sarawak, Malaysia

3 Graphene & Advanced 2D Materials Research Group (GAMRG), School of Engineering and Technology, Sunway University, Petaling Jaya, Selangor, Malaysia

4 State Key Laboratory of ASIC and System, SIST, Fudan University, Shanghai 200433, China

5 Graduate School of Information Science & Electrical Engineering, Kyushu University, Fukuoka 819-0395, Japan

characteristics such as high specific surface area, abundant porosity, good hydrophilicity, and good conductivity [5]. In recent years, the biochars produced from thermochemical decomposition of biomass have received significant attention especially for the area of soil amendment [6], carbon sequestration [7], and waste water treatment [8, 9]. However, there are limited research focuses on the application of biochar for energy storage [10].

Biomass stands a greater chance of prevailing as a good source for the production of biochar due to its availability globally [11]. Sugarcane bagasse [9], durian rind [12], mangosteen peel [8], coconut shell [13], corn stover [14], rice husks [15, 16] olive husk [17], pine [18], Miscanthus [19], and sewage sludges [20] are some types of biomass used for biochar production.

There are different methods of biochar production, but the commonly used methods are high-temperature pyrolysis, hydrothermal carbonization, and microwave pyrolysis [21–23]. Each method has different advantages and drawbacks. High-temperature pyrolysis usually works at temperature beyond 500 °C and relatively causes high energy consumption. However, this method is still being opted by the researchers due to its simplicity and less production time. Different from high-temperature pyrolysis, hydrothermal carbonization normally applied under lower temperature. Thus, the energy consumption is low. In addition, the surfaces of biochar produced by this method owing more active sites which are beneficial for next step treatment [5]. Unfortunately, the products of this low temperature process possess low carbon content which limits its application in various areas due to low conductivity. Microwave pyrolysis stands over other methods in terms of efficiency, time consumption, and clean process route. But the major problem is the higher production cost compared with other abovementioned methods [24].

The characteristics of biochars produced primarily dependent on the process conditions and the origin of biomass. Normally, the biochar directly obtained from biomass pyrolysis poses low specific surface area, poor porosity, and inadequate surface functional groups [25]. In order to expand its applications, several modifications need to be done. The properties of biochar can easily be tuned by the appropriate activation or functionalization. Chemical activation is one of the common methods used to improve the specific surface area and of pore structure of carbon materials [26]. Common chemical activating agents used are KOH, NaOH, K_2CO_3, $ZnCl_2$, and H_3PO_4. Normally, the chemicals are impregnated into the biomass prior to pyrolysis process [27]. Chemical activation can be performed in relatively lower temperatures and results in a biochar with high porosity and surface area [28]. However, the variables during activation process such as activation temperature, the type of activating agent, and feedstock type may significantly affect the porosity and surface area of produced biochar. For instance, Angin et al. (2013) in

their study found that the surface area and pore volume of the biochar from safflower seed were significantly increased with increasing the activation temperature (600–900 °C) and impregnation ratio (1:1–4:1) [29].

Herein, novel CS-BMO (CS-BMO 500, CS-BMO 600, and CS-BMO 700) and WR-BMO (WR-BMO 500, WR-BMO 600, and WR-BMO 700) samples were fabricated respectively via self-purging pyrolysis with coconut shell and watermelon rind as the carbon source at 500 °C, 600 °C, and 700 °C, wherein CS-BMO 600 and WR-BMO 600 materials were resulted in good electrochemical performance (Table 1).

$CoFe_2O_4$ and $NiFe_2O_4$ ratio used in the experiments was fixed to 1:1 (in grams). Pyrolysis temperature was fixed to 20 min for all samples. Sonochemical treatment using probe sonicator for 30 min at 70% frequency for all samples before pyrolysis

2 Experimental

2.1 Materials and Method

Coconut shell powder (600 mesh) was purchased from Kuala Perak Coconut Industries, Malaysia. Watermelon rinds were obtained from local markets. The residue flesh was removed, then the rinds were cut into small pieces and dried in the oven at 80 °C for 24 h. The oven-dried watermelon rind was powdered using a conventional grinder then stored in airtight container. All chemicals and reagents were of analytical grade and used as received without any further purification. Iron nickel oxide, Fe_2NiO_4, cobalt iron oxide, and $CoFe_2O_4$ were purchased from Sigma–Aldrich, Malaysia. Potassium permanganate, $KMnO_4$, was purchased from R&M Chemicals. The bench top pH meter (brand: SI Analytics Model: Lab 845) was employed to control pH of the samples. The programmable muffle furnace model WiseTherm, FP-03, 1000 °C, 3L was used to prepared biochar. Nickel foam of uniform thickness (1.6 mm, bulk density—0.45 gcm^{-3}, porosity—95%) was supplied by Sigma–Aldrich, Malaysia.

Table 1 Sample preparation for CSB, WRB, CS-BMO, and WR-BMO

Sample	Pyrolysis temperature (°C)
CSB	600
WRB	600
CS-BMO 500	500
CS-BMO 600	600
CS-BMO 700	700
WR-BMO 500	500
WR-BMO 600	600
WR-BMO 700	700

2.2 Preparation of CS-BMO and WR-BMO biomass

One hundred milliliters of each analytical grade binary metal oxide of iron nickel oxide, Fe_2NiO_4 (0.4 g), and cobalt iron oxide, $CoFe_2O_4$ (0.4 g), solutions were transferred into 1L Pyrex laboratory beaker, followed by 100 ml potassium permanganate ($KMnO_4$) for optimum functionalization process. This solution was mixed uniformly prior the addition of 200 ml solution containing 100 g coconut shell powder into the 200 ml mixture of 1-L Pyrex laboratory beaker. The mixture was then sonicating for 30 min with 70% frequency using probe sonicator (brand: QSONICA). The mixture was then dried in oven for 48 h at 70 °C to obtain metal ion-coconut shell biomass. The above methods were repeated for the preparation of binary metal oxide-watermelon rind biomass.

2.3 Synthesis of CS-BMO and WR-BMO biochar

The pyrolysis processes of the CS-BMO and WR-BMO biomass were performed in the limited oxygen condition in programmable muffle furnace model WiseTherm, FP-03, 1000 °C, 3L. Closed crucibles containing 20 g of dried CS-BMO and WR-BMO biomass were kept in the middle of the furnace, and the furnace's door was then closed tightly. The vacuum pump was then connected to the syngas effluent's tip located at the top of the furnace to suck out the air inside the furnace to promote limited oxygen condition throughout the pyrolysis process. The pyrolysis process was carried out according to the required time and temperature. The furnace was allowed to cool down upon completion of the pyrolysis until room temperature was attained before removing the crucible from the furnace. The total amounts of CS-BMO and WR-BMO produced were weighed and then washed with distilled water until pH neutral obtained and dried in the oven for 24 h at 70 °C.

2.4 Yield of CSB, WRB, CS-BMO, and WR-BMO

A range of pyrolysis temperatures (500 °C, 600 °C, and 700 °C) were employed in order to determine the optimum temperature for the production of CS-BMO and WR-BMO biochar. The holding time was fixed at 20 min by taking the middle holding time according to the research done by Thines et al. (2017) using durian rind as biomass. The yield of CS-BMO and WR-BMO biochar produced was determined by employing Eq. (1)

$$\text{Yield } (\%) = \frac{Wi}{Wf} \times 100 \tag{1}$$

where Wi represents the initial dry weight of CS-BMO and WR-BMO biomass in gram which is used as feed while Wf

represents the final dry weight (g) of CS-BMO and WR-BMO biochar produced after the pyrolysis process.

2.5 Characterization of CS-BMO and WR-BMO biochar

Characterization studies of both as-synthesized CS-BMO and WR-BMO samples were performed in order to analyze their surface structure, chemical composition and decomposition temperature crystallinity, and surface area. The surface morphology and elemental composition were studied using JEOL:JSM-7800F microscope fitted with energy dispersive X-ray analyzer (FESEM-EDX). The surface structure and functional groups present in CS-BMO and WR-BMO samples were characterized and evaluated by Fourier transform infrared (FTIR) spectroscopy (Spotlight 200i FTIR Microscope System). The samples were scanned in the range of 4000–400 cm^{-1}. In this analysis, KBr pellets of the samples were prepared by mixing KBr powder with the samples at the ratio of 1:10. The thermogravimetric analysis (TGA) was used to identify the mass change of the sample as a function of temperature by using TGA 55. In this analysis, a small sample size was used in the range of 10 to 200 mg which was heated at temperatures ranging from 25 to 900 °C at 20 °C/min decomposition rate. The crystalline nature and phase identification of the samples were determined by using X-ray diffractometer (model: PANanalytical Empyrean Diffractometer) equipped with Cu K-α radiation (λ =1.5418 Å) at a scan rate 0.2 s^{-1}, step 0.05° over 2ø, 5° to 90°. The surface area with pore volume and pore size of CS-BMO and WR-BMO samples were determined by using Brunauer–Emmett–Teller (BET) (model: NOVAtouch Quantachrome) at N_2 condition.

2.6 Electrochemical measurements

The electrochemical performance of the sample electrode was assessed using cyclic-voltammetric and galvanostatic charge discharge methods (VersaSTAT-3F). A 3M KOH, saturated calomel electrode (SCE), and platinum wire were used as the electrolyte, reference electrode, and counter electrode respectively. The sample electrode (dimension 1 cm × 1 cm) was dipped in the electrolyte prior to the analysis. Cyclic voltammetry (CV) was used to determine the electrochemical parameters of the electrode. The CV voltamoggrams were recorded within certain potential windows at different scan rates. The specific capacitance, Cs (Fg^{-1}) of the electrodes was obtained by using the Eq. (2) [30]. While the galvanostatic charge discharge (GCD) analysis was performed at different current density within the specified potential windows.

$$Cs = (\int IdV)/vm\Delta V \tag{2}$$

The specific capacitance, C from GCD can be calculated by using Eq (3) [3].

$$C = It/(m\Delta V) \tag{3}$$

where I (A) is the response current, V (V) is applied potential, ΔV (V) is the potential window, v (mVs^{-1}) is the scan rate, and m (g) is the mass of active material in the electrode. The energy density calculations were done with Eq. (4) [31].

$$E = 0.5 \times Cs \times V^2 \tag{4}$$

3 Results and discussion

3.1 Yield of CSB, WRB, CS-BMO, and WR-BMO

Figure 1 demonstrates the effects of pyrolysis temperature on the yield of CSB, WRB, CS-BMO, and WR-BMO samples produced at 500 °C, 600 °C, and 700 °C. It is clearly shown that, as the pyrolysis temperature increases, the yield of biochar produced decreases as in accordance with the research done by previous researchers [32–34]. This is due to the thermal cracking of hydrocarbon materials leading to the increase of liquid and gaseous. Comparing the results, it can be seen that WR-BMO samples have the highest yield followed by CS-BMO, WRB, and CSB samples. On a mass basis, the biochar's yield ranged from 19.6 to 25%, 22.1 to 31.7%, 23.3 to 36%, and 31.6 to 39.5% of initial dry weight, respectively, for CSB, WRB, CS-BMO, and WR-BMO samples.

During pyrolysis process, the temperature kept rising and was then held at the required temperature for several minutes or hours (depending on pyrolysis time) before cooling down to room temperature. The weight loss of the samples below 250 °C was corresponding to the loss of moisture and water hydration. While the biomass begins to decompose at the temperature above 250 °C [33].
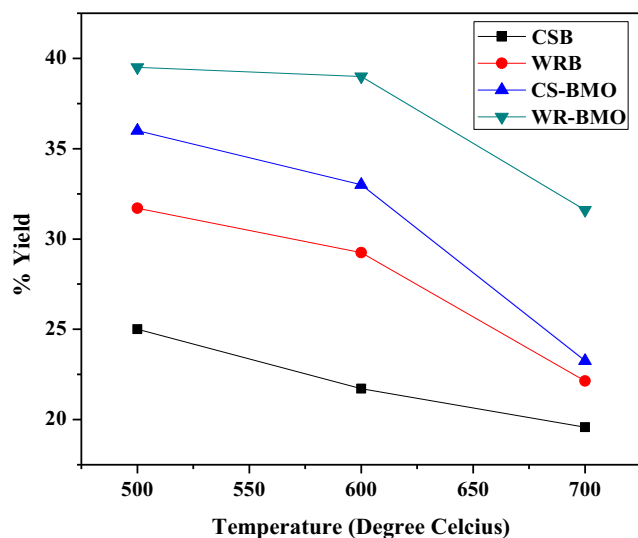

Fig. 1 The yield of prepared CSB, WRB, CS-BMO, and WR-BMO

3.2 FESEM analysis

The structural and surface morphologies of CSB, WRB, CS-BMO, and WR-BMO samples were further analyzed using FESEM. Figure 2 shows the images of CSB (produced at 600 °C), WRB (produced at 600 °C), CS-BMO, and WR-BMO produced at 500, 600, and 700 °C at ×10,000 magnification. In Fig. 2a, it clearly indicates the coconut shell biochar has a folded rough surface with a structure of irregular shape throughout the sample as in agreement with the research done by Sarswat and Mohan (2016) [35]. In addition, there is no sign of formation of pores on CSB surface. The formation of rough cavities over the surface of CSB and CS-MBO was more related to the breakdown of lignocellulosic material at high temperature [36]. The surface changes after $CoFe_2O_4$ and Fe_2NiO_4 loaded and functionalization with 0.4M $KMnO_4$ are visible in Fig. 2b–d. Some cavities are blocked with binary metal oxide particles and potassium permanganate particles.
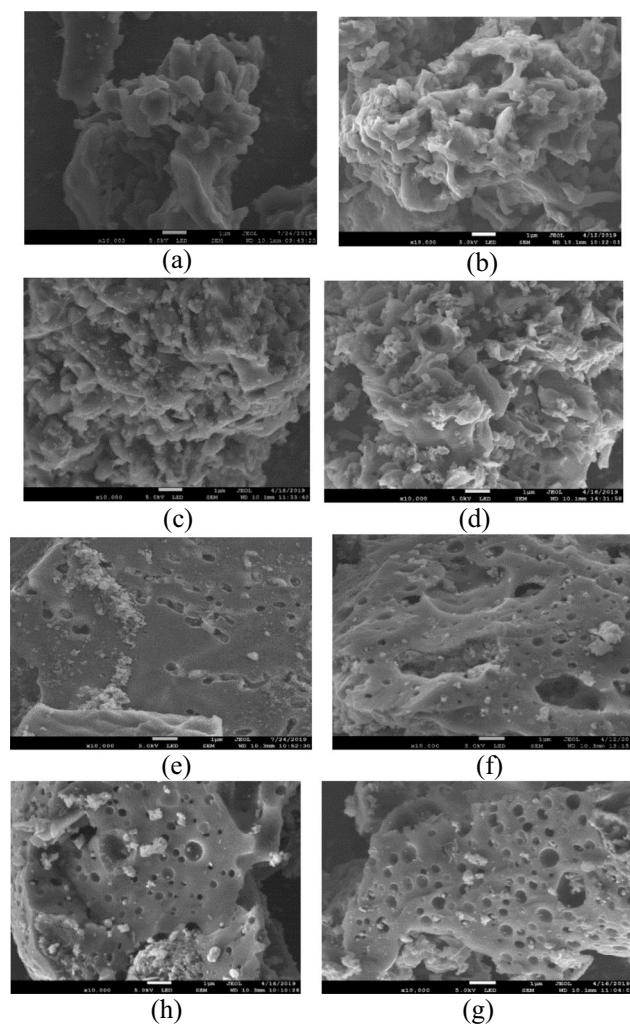

Fig. 2 FESEM images of **a** CSB, **b** CS-BMO 500, **c** CS-BMO 600, **d** CS-BMO 700, **e** WRB, **f** WR-BMO 500, **g** WR-BMO 600, and **h** WR-BMO 700

KMnO$_4$ has significant impacts on specific surface area of produced biochar since alkaline modification increases the surface area and oxygen-containing functional groups on the surface of biochar [37, 38]. Figure 2 e–h show FESEM images of WRB (produced at 600 °C) and WR-BMO produced at 500, 600, and 700 °C. As compared with FESEM image of CSB, WRB has smooth surfaces with distinctive pores shown in Fig. 2e. The pore diameter present on the structure of the WR-MBO seems to be larger as the pyrolysis temperature increases. This is attributed to the high activation temperature of pyrolysis which can give a wider microporosity. The pores formation might be due to the volatile matter escaping during the high temperature of pyrolysis [12].

3.3 EDX analysis

Energy dispersive X-ray spectroscopy analysis (EDX) was used to identify the elemental composition present in CSB, WRB, and CS-BMO and WR-BMO samples. Table 2 shows the EDX results of CSB, WRB, and both synthesized CS-BMO and WR-BMO samples with their respective quantitative weight values. Figure 3 a, b show the EDX spectrum of CSB and WRB which indicated the presence of C, O, Si, P, K, and Na. The binary metal oxide loading on carbon is confirmed by the presence of iron, cobalt, and nickel peaks in CS-BMO and WR-BMO samples as demonstrated in Table 2. With the increment of pyrolysis temperature, increasing trends in carbon components of the CS-BMO and WR-BMO were observed. Higher volatiles were also released with rising temperature that leads to reduction of oxygen content. However, the reduction range was small and non-uniform, which infers that oxygen content involved in the prudent units of the scission process was evaporated at the lower temperature zone [39].

3.4 FTIR analysis

Fourier transform infrared spectroscopy (FTIR) was performed to study the functional groups present in CSB, WRB, and both synthesized CS-BMO and WR-BMO at different pyrolysis temperature. A small peak was observed at 3600 cm^{-1} for CSB in Fig. 4a which indicates the adsorbed water and the presence of moisture in the samples [40, 41]. The absorption peak at 1606, 1616, 1588, and 1574 cm^{-1} for CSB, CS-BMO 500, CS-BMO 600, and CS-BMO 700, respectively, corresponds to C=C stretching vibration [42]. The peak of 1052, 1076, and 1071 cm^{-1} for CSB, CS-BMO 500, CS-BMO 600, and CS-BMO 700 represented stretching vibration of C–OH alcoholic group and carboxylic acids and the involvement of C–O–C lactone structure [43]. As seen from Fig. 4a, a broad band for CS-BMO 500 is exhibited at around 3500 cm^{-1}, and this corresponds to the O–H stretching vibration of hydroxyl group in cellulose molecules along with the intramolecular and intermolecular hydrogen bonds. A narrow band at around 2309 and 2352 cm^{-1}, respectively, for CSB and CS-BMO 500 attributes to CO$_2$ bond present in the coconut shell. Both of the bands mentioned above are absent for both CS-BMO produced at 600 and 700°C. This indicates lesser adsorption bands due to the disappearance of these particular functional groups after high temperatures of pyrolysis, and the conversion of cellulosic material into a carbon material which is magnetized [44, 45]. However, the band gets narrow and disappears for CS-BMO 600 and CS-BMO 700, respectively. Furthermore, a small and narrow band seen at around 880 cm^{-1} could indicate a bending vibration of the C–H bond in the high degree of the substitution of the aromatic ring [42]. Besides, all of the CS-BMO samples also exhibited a peak at around 619 cm^{-1} ascribed to Fe–O stretching vibration derived from nickel iron oxide (Fe$_2$NiO$_4$) and cobalt iron oxide (CoFe$_2$O$_4$) [46].

Table 2 Chemical composition of CSB, WRB, and as-synthesized CS-BMO and WR-BMO samples under different pyrolysis temperature

Elements	Chemical compositions in weight (%)							
	CSB	WRB	CS-BMO 500	CS-BMO 600	CS-BMO 700	WR-BMO 500	WR-BMO 600	WR-BMO 700
C	60.94	49.96	65.37	72.09	76.32	68.31	75.86	77.42
O	29.39	24.26	20.12	13.17	15.97	16.58	15.06	15.46
Si	6.01	0.48	-	-	-	-	-	-
P	0.19	1.30	-	-	-	-	-	-
K	2.18	19.49	-	-	-	-	-	-
Na	1.29	0.22	-	-	-	-	-	-
Mn	-	-	6.09	2.63	5.75	5.59	5.73	3.13
Fe	-	-	4.38	7.93	0.20	0.44	0.48	0.32
Co	-	-	2.18	1.95	0.11	0.12	0.22	0.23
Ni	-	-	0.37	0.54	0.16	0.22	0.16	0.31

(a)

(b)
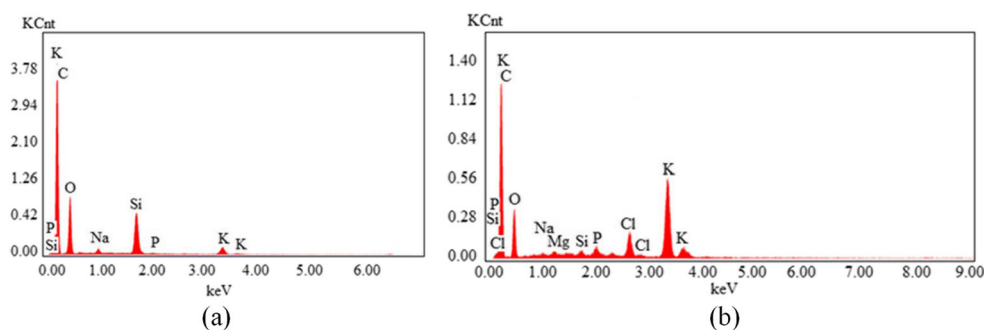
For WRB (in Fig. 4b), it clearly shows the absorption band at 3200–3600 cm^{-1} that could be related to O–H vibration and N–H stretching. This is due to the composition of watermelon rind which contains protein, pectin, carotenoids, and cellulose,

(a)

(b)
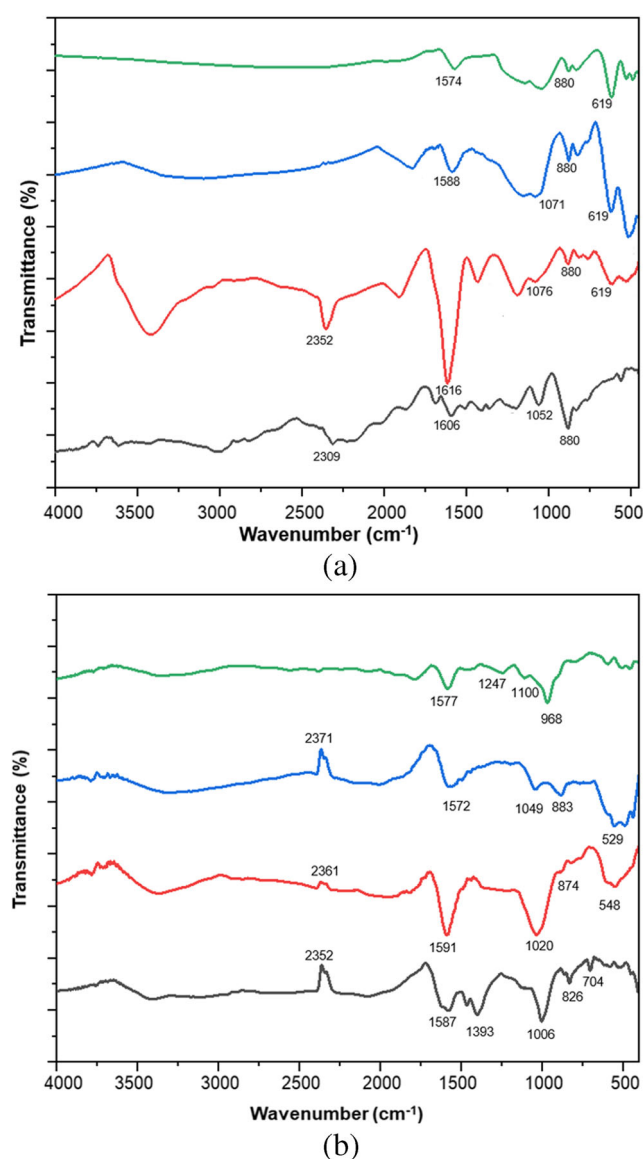
Fig. 4 FTIR spectra of **a** CSB, CS-BMO 500, CS-BMO 600, and CS-BMO 700 and **b** WRB, WR-BMO 500, WR-BMO 600, and WR-BMO

which converted to hydroxyl, amine, and carboxylic groups [47]. The bands at 2352, 2361, and 2371 cm^{-1} for WRB, WR-BMO 500, and WR-BMO 600 were related to the C–H stretching of methyl groups, and the band disappeared for WR-BMO 700. A broad adsorption band exhibited at around 3400 cm^{-1} for WR-BMO produced at 500 °C corresponding to the existence of O–H groups and N–H stretching vibration. This is due to the watermelon rind being rich in hydroxyl (cellulose, polysaccharide), amine (amino acid), and carboxylic (pectin groups). The peaks around 1587, 1591, 1572, and 1577 cm^{-1} for WR, WR-BMO 500, WR-BMO 600, and WR-BMO 700, respectively, attributed to the C=C stretching vibration. The broad and short band seen at around 1400 cm^{-1} to 1300 cm^{-1} refers to the C–H in plane bending vibrations in methyl and methylene groups [44]. Another peak starting around 1006, 1020, 1049, and 1100 cm^{-1} for WR, WR-BMO 500, WR-BMO 600, and WR-BMO 700, respectively, corresponded to the C–O stretching in alcohols or ester groups for. The band present at 548 and 529 cm^{-1} confirms the formation of Fe–O bond which attributes the presence of iron oxides from both nickel iron oxide and cobalt iron oxide used in the preparation of the sample for its magnetic properties. Two obvious bands around 1630- and 1400-cm^{-1} regions, which were observed in all carbons and magnetite impregnated carbons, correspond to ring vibration in a large aromatic skeleton or C=O stretching modes in aromatic ring structure [48, 49].

3.5 TGA analysis

Furthermore, thermogravimetric analysis (TGA) was carried out for CSB, WRB, and both as-synthesized CS-BMO and WR-BMO samples with different pyrolysis temperatures (500, 600, and 700 °C). TGA studies were performed in which the variation of CSB, WRB, CS-BMO, and WR-BMO sample's mass with determined as a function of temperature 25 to 1000 °C at 10° C min^{-1}·Fig. 5a illustrated the TGA curves corresponding to the mass loss of CSB, WRB, and as-synthesized CS-BMO and WR-BMO samples with respect to the temperatures.

The weight of CSB decreased slightly with increasing temperature from 27 to 600 °C. The graph can be divided into 3

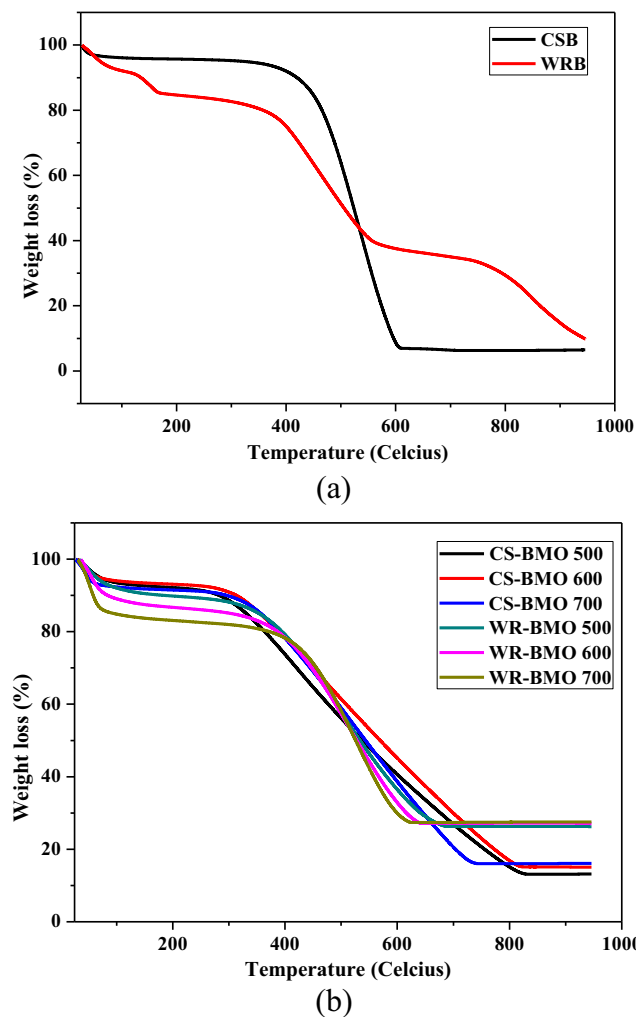Fig. 5 TGA thermograms of **a** CSB and WRB and **b** CS-BMO and WR-BMO

Fig. 6 XRD patterns of **a** CSB and CS-BMO and **b** WRB and WR-BMO samples

stages. In the first stage, the decreasing slope corresponds to the removal of volatile matter, moisture, and other impurities. The second stage of decomposition occurs around 250 to 600 °C approximately to 88.72% weight loss which can be attributed to the decomposition of biochar [50]. Nevertheless, the third stage of decomposition happened from 600 to 900 °C indicates the presence of fixed carbon and non-combustion product [13]. For WRB, the decomposition stages can be roughly divided into four stages. The first stage appeared at around 27 to 150 °C which corresponded to the evaporation of moisture presence in the WRB. The second stage of decomposition occurred at around 150 to 300 C. This might be due to the decomposition of bound water in WRB [51]. The major weight loss occurred at around 300 to 650 °C which might be due to the decomposition of chemical activating agent and binary metal oxides presence in the WRB sample. The final decomposition stage around 650 to 945 °C might be corresponded to the fixed carbon and other non-combustion element presence in the sample.
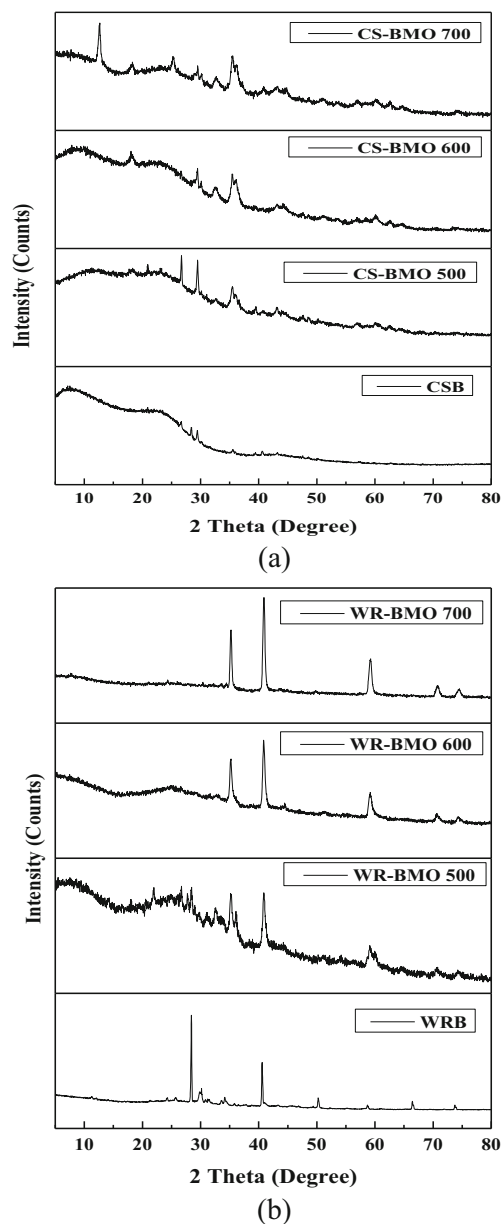
For CS-BMO samples, the decomposition trends were found to be same as CSB sample as in Fig. 5. The first stage of decomposition appeared at around 29, 31, and 28 °C to approximately 200 °C for CS-BMO 500, CS-BMO 600, and CS-BMO 700, respectively. This weight loss attributed to the removal of volatile matter, moisture, and other impurities' presences in CS-BMO samples. The major weight loss occurs at second decomposition stage at 200 to 850 °C (79.17%), 825 °C (77.95%), and 750 °C (75.39%) for CS-BMO 500, CS-BMO 600, aand CS-BMO 700, respectively, which is due to the decomposition of biochar and other activating agents and binary metal oxides presence in the samples [50].

TGA curves for WR-BMO 500, WR-BMO 600, and WR-BMO 700 in Fig. 5 show the weight of WR-BMO samples

Table 3 BET surface area, pore volume, and average pore radius for CSB, WRB, CS-BMO, and WR-BMO

Samples	BET surface area (m²/g)	Pore volume (cc/g)	Average pore radius (nm)
CSB	67.035	$6.6531e^{-002}$	1.9849
WRB	12.698	$1.9430e^{-002}$	3.0603
CS-BMO 500	312.021	$1.7053e^{-001}$	1.0931
CS-BMO 600	322.142	$1.8334e^{-001}$	1.1383
CS-BMO 700	288.470	$0.18978e^{-001}$	1.3157
WR-BMO 500	274.853	$1.8934e^{-001}$	1.3777
WR-BMO 600	441.021	$0.28386e^{-001}$	1.3370
WR-BMO 700	429.230	$0.28654e^{-001}$	1.3351

decreased at temperature around 32 to 945 °C, which is slightly higher than WRB sample. Three main decomposition stages can be observed from recorded thermo-analytical curves which can be described as follows: stage 1 from ~32

Table 4 The capacitive performance of CSB, WRB, Cs-BMO 600, and WR-BMO 600

Materials	Scan rate (mVs⁻¹)	Cs (Fg⁻¹)	Energy density (Wh Kg⁻¹)
CSB	5	79.97	39.98
	10	41.40	20.70
	20	29.20	14.60
	30	24.13	12.06
	40	19.67	9.84
	50	16.51	8.26
	100	8.52	4.26
WRB	5	117.58	58.79
	10	58.50	29.25
	20	45.36	22.68
	30	40.34	20.17
	40	33.37	16.69
	50	28.06	14.03
	100	14.31	7.16
CS-BMO 600	5	111.66	13.96
	10	57.41	7.17
	20	50.40	6.30
	30	46.20	5.78
	40	41.40	5.18
	50	36.91	4.61
	100	19.90	2.49
WR-BMO 600	5	152.09	19.01
	10	74.82	9.35
	20	48.36	6.05
	30	32.10	4.01
	40	26.20	3.28
	50	21.97	2.75
	100	11.29	1.41

to ~200 °C (mass loss around 14%) resulted in the removal of moisture presence in WR-BMO samples. Second decomposition stage was observed from ~200 to ~650 °C which represents the greatest weight loss recorded at ~ 63%, ~59%, and ~54% for WR-BMO 500, WR-BMO 600, and WR-BMO 700, respectively. Actual thermal behavior was similar to other studies [52]. Final stage of mass loss occurs at ~650 to ~945 °C (~10%, ~13%, and ~17%, respectively, for WR-BMO 500, WR-BMO 600, and WR-BMO 700, respectively) which might correspond to decomposition of carbonaceous matter in WR-BMO samples.

3.6 XRD analysis

X-ray diffraction is an applicable tool to analyze biomass crystallinity and biochar structure. The XRD patterns obtained for CSB, WRB, CS-BMO, and WR-BMO samples are shown in Fig. 6a, b. XRD diffractogram of CSB in Fig. 6a indicates the wide peak at 29.44° which showed that carbon graphite was present in the CSB sample [53]. XRD pattern of WRB in Fig. 6b shows peaks of high intensity around 29.80 ° and 40.58 °. However, there were no characteristic XRD peaks in CSB sample suggesting that CSB was amorphous [54].

For CS-BMO samples in Fig. 6a, the peak around 35.5° was observed. As the pyrolysis temperature increased, the peak's intensity also increased indicating that the crystalline structure of graphitized carbon in CS-BMO 700 sample is higher than CS-BMO 600 and CS-BMO 500. In addition, other diffraction peaks also observed in CS-BMO samples (26.71° and 29.47° for CS-BMO 500; 18.17° and 60.15° for CS-BMO 600; 12.62, 25.30 and 32.66 for CS-BMO 700) which might be due to the presence of $KMnO_4$ and binary metal oxides in the sample.

XRD trends of WR-BMO samples in Fig. 6b display an increase in diffraction peak strength at 35° corresponding to the crystalline structure of graphitized carbon as the pyrolysis temperature rises from 500 to 700 °C [55]. Same with WRB sample, the diffraction peak at around ~40.8° is also observed for WR-BMO 500, WR-BMO 600, and WR-BMO 700 samples. On another note, as the pyrolysis temperature increases,
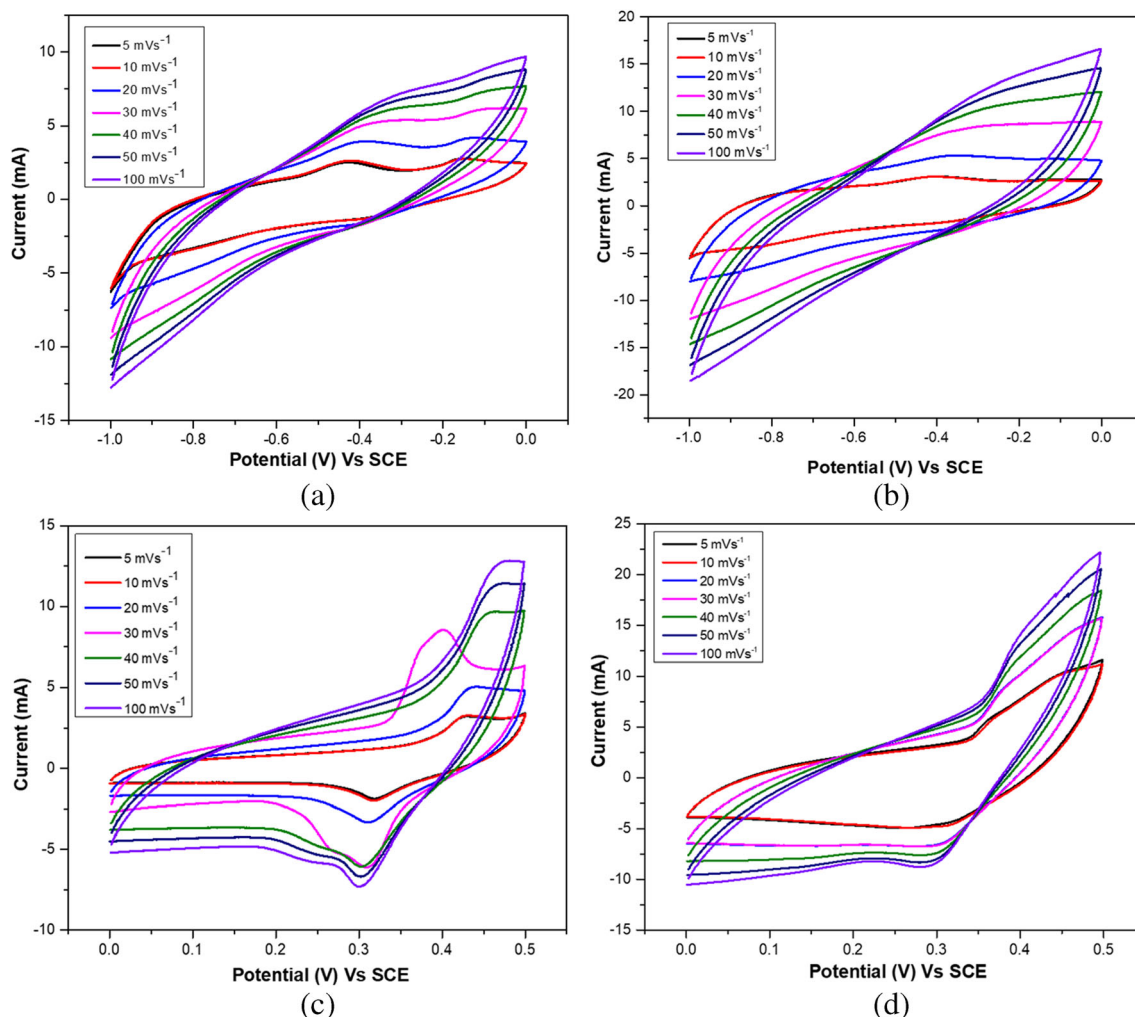
Fig. 7 Cyclic voltammogram curve of **a** CSB, **b** WRB, **c** CS-BMO 600, and **d** WR-BMO 600

more diffraction peaks are observed in the samples, for example, the appearance of diffraction peaks at 59.14° and 70.73° for WR-BMO 600 and 59.26°, 70.81°, and 74.46° for WR-BMO 700 which indicates the degree of crystallinity [56].

3.7 BET surface area

The specific surface area was determined by the BET method since these values are considered very important due to the dominance of the surface properties [12]. The BET surface area values, along with the pore volume and average pore radius for CSB, WRB, CS-BMO, and WR-BMO, are summarized in Table 3. The increase in the BET surface area is led to a reduction in the average pore radius. This is in agreement with the research done by Chen et al. (2011). On the other hand, it is reported that, with the incorporation of $CoFe_2O_4$ and Fe_2NiO_4 and activation with $KMnO_4$, the BET surface area and total pore volume were increased. This might happen due to the decomposition of the oxygen functional groups during pyrolysis process in the muffle furnace with vacuum

condition [57]. The highest BET surface area of CS-BMO was obtained at 322.142 m^2/g found at the sample produced at 600 °C as compared with BET surface area of CSB sample without any activation and metal oxide loading was 67.035 m^2/g.

The highest BET surface area of 441.021 m^2/g for WR-BMO was also found for the sample produced at 600 °C. While the BET surface area for WRB sample was found to be 12.698 m^2/g. These results prove that the surface functionalization and binary metal oxide loading during biomass preparation provided additional forces in rising BET surface area [58].

3.8 Electrochemical analysis

The electrochemical performance of CSB, WRB, CS-BMO 600, and WR-BMO 600 was evaluated using cyclic voltammetry (CV) and galvanostatic charge discharge (GCD) methods. CS-BMO 600 and WR-BMO 600 samples were chosen to perform electrochemical analysis due to their greatest specific surface area value since the surface area has proportional
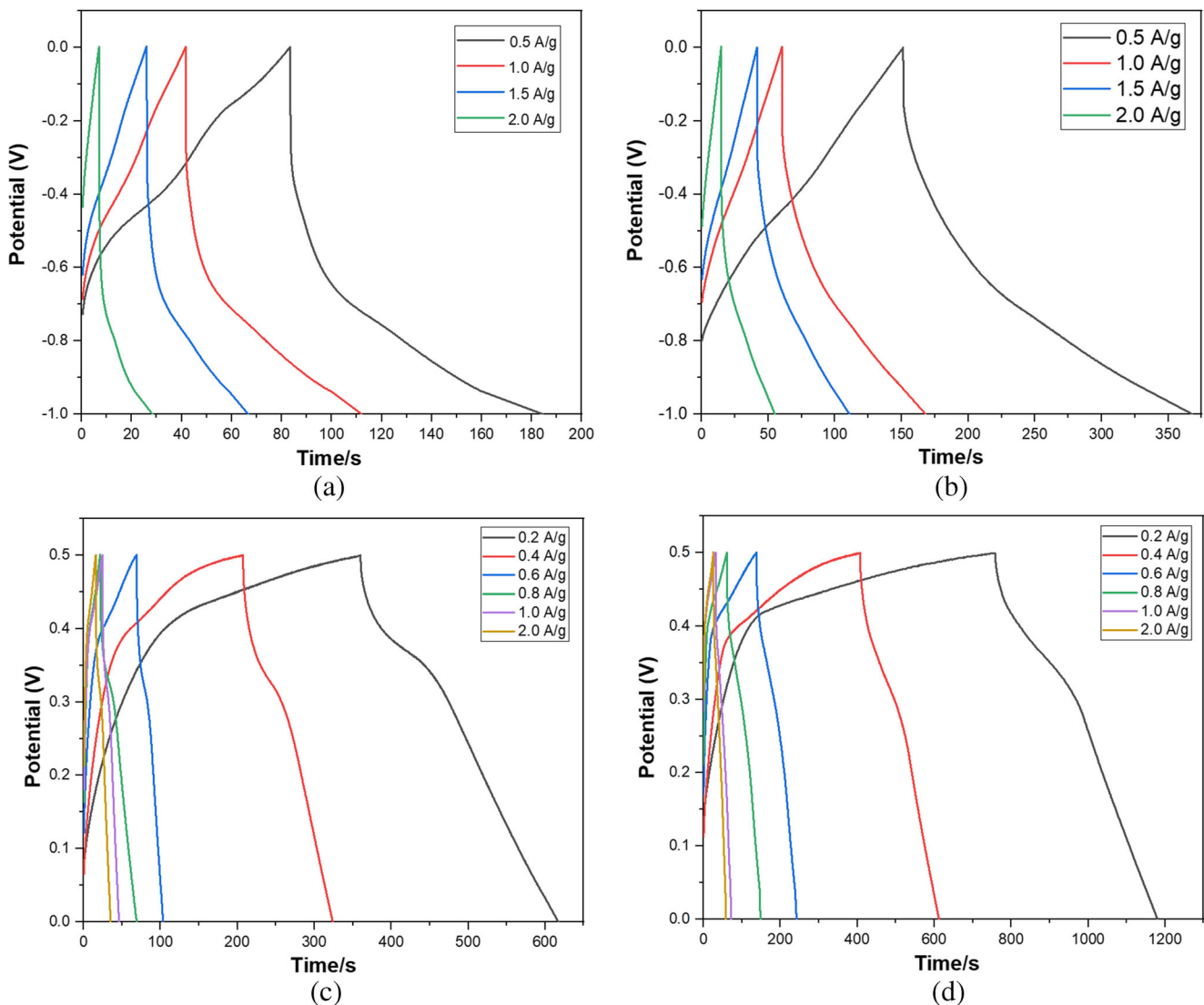
Fig. 8 Galvanostatic charge-discharge (GCD) curve of **a** CSB, **b** WRB, **c** CS-BMO 600, and **d** WR-BMO 600

relationship [59]. The cyclic voltammetry responses samples at different scan rates (5–100 mVs^{-1}) over the potential window −1–0 V for CSB and WRB, while 0–0.5 V for CS-BMO 600 and WR-BMO 600 in a standard three-electrode cell are presented in Fig. 7a–d. As shown in Fig. 7a, b, CSB and WRB present an approximately rectangular CV shape indicating typical feature of a double layer capacitor [1–3]. CV curve integral area of WR-BMO 600 is larger than CS-BMO 600 as displayed in Fig. 7c, d indicating the WR-BMO 600 has better electrochemical performance than CS-BMO 600 [2, 30]. A vertical bending was observed at higher scan rate for the voltammograms in Fig. 7d compared with the voltammograms in Fig. 7c. This implies strong pseudocapacitive feature of WR-BMO 600 sample [30, 45]. In addition, the larger areas of the closed curves implied higher specific capacitances. Clearly, the CV curve area of WR-BMO 600 was the largest among the four samples and meant that WR-BMO 600 obtained the largest specific capacitance. The better electrochemical performance

of binary metal oxide loaded biochar was because of the greater surface area and pore volume which reinforced electron transport and mobility of charge carriers. All electrodes showed a similar trend of decreasing Cs value when scan rate increases. The reason for the highest Cs at the low scan rate is that the ions have longer time to penetrate and resided at electrode pores which is favorable to form electric double layer [30, 60]. The measured specific capacitance from CV for CSB, WRB, CS-BMO 600, and WR-BMO 600 calculated from CV curves is demonstrated in Table 4.

Figure 8 a–d show a plot of galvanostatic charge-discharge (GCD) results for four samples for various current density. According to the calculation of discharge time, the specific capacitance of CSB and WRB is at current density of 0.5 A g^{-1}, 46.5 Fg^{-1}, and 106 Fg^{-1} respectively. The shape of GCD curves for WRB is nearly symmetrical, and isosceles triangle is formed at various current densities. This shows that WRB has an ideal capacitive behavior [61]. The measured specific

capacitance for CS-BMO 600 and WR-BMO 600 is slightly higher than those CSB and WRB. The highest specific capacitance of CS-BMO 600 was recorded 103.2 Fg^{-1} at 0.2 Ag^{-1} current density. Among all, WR-BMO 600 has recorded the highest specific capacitance of 174.4 Fg^{-1} at 0.2 Ag^{-1} current density, and the lowest specific capacitance of 78 Fg^{-1} was recorded at 2.0 Ag^{-1} current density. The specific capacitance turns to decrease at higher current density due to the narrow pore size of the micropores hindering the effective diffusion of electrolyte ions, reducing the accumulation of electrolyte ions on the interface [47].

4 Conclusion

The property biochars are dependent on the types of biomass and pyrolysis temperature. The experiment revealed the optimum pyrolysis temperature for both CS-BMO and WR-BMO was 600 °C. EDX analysis indicated that the density of carbon functional group increased at the higher pyrolysis temperature for both CS-BMO and WR-BMO samples. FESEM results also showed that well dispersed metal oxide particles on the biomass surfaces prove the significance of using sonochemical treatment by using probe sonicator. FTIR analysis shows that lesser adsorption bands in the CS-BMO and WR-BMO samples with higher pyrolysis temperature due to the disappearance of these particular functional groups after high temperatures of pyrolysis and the conversion of cellulosic material into a carbon material which are magnetized. XRD analysis shows that, as the pyrolysis temperature increases, more diffraction peaks are observed in the samples. BET surface area results show that the binary metal oxide loaded biochar, CS-BMO, and WR-BMO were successfully produced with high BET surface area of 322.12 m^2/g for CS-BMO produced at 600 °C and 441.021 m^2/g for WR-BMO produced at 600 °C. Cyclic voltammetry study highlighted that the WR-BMO 600 (152.09 Fg^{-1}) is superior to the CSB, WRB, and CS-BMO 600. Therefore, this novel approach in the development of waste material into a more valuable and innovative product provides a new dimension for the carbon and waste treatment industry to the functional materials for various fields specifically energy storage devices which currently under exploration.

References

1. Agudosi ES, Abdullah EC, Numan A, Mubarak NM, Aid SR, Benages-Vilau R, Gómez-Romero P, Khalid M, Omar N (2020) Fabrication of 3D binder-free graphene NiO electrode for highly stable supercapattery. Sci Rep 10(1):11214

2. Dong J, Li S, Ding Y (2020) Anchoring nickel-cobalt sulfide nanoparticles on carbon aerogel derived from waste watermelon rind for high-performance asymmetric supercapacitors. J Alloys Compd 845:155701

3. Xie K, Zhang M, Yang Y, Zhao L, Qi W (2018) Synthesis and supercapacitor performance of polyaniline/nitrogen-doped ordered mesoporous carbon composites. Nanoscale Res Lett 13(1):163

4. Kalyani P, Anitha A (2013) Biomass carbon and its prospects in electrochemical energy systems. Int J Hydrog Energy 38(10):4034–4045

5. Wang J-R, Wan F, Lü Q-F, Chen F, Lin Q (2018) Self-nitrogen-doped porous biochar derived from kapok (Ceiba insignis) fibers: Effect of pyrolysis temperature and high electrochemical performance. J Mater Sci Technol 34(10):1959–1968

6. Lehmann J, Rillig MC, Thies J, Masiello CA, Hockaday WC, Crowley D (2011) Biochar effects on soil biota – a review. Soil Biol Biochem 43(9):1812–1836

7. Smider B, Singh B (2014) Agronomic performance of a high ash biochar in two contrasting soils. Agric Ecosyst Environ 191:99–107

8. Ruthiraan M, Abdullah EC, Mubarak NM, Noraini MN (2017) A promising route of magnetic based materials for removal of cadmium and methylene blue from waste water. J Environ Chem Eng 5(2):1447–1455

9. Noraini MN, Abdullah EC, Othman R, Mubarak NM (2016) Single-route synthesis of magnetic biochar from sugarcane bagasse by microwave-assisted pyrolysis. Mater Lett 184:315–319

10. Magnacca G, Guerretta F, Vizintin A, Benzi P, Valsania MC, Nisticò R (2018) Preparation, characterization and environmental/electrochemical energy storage testing of low-cost biochar from natural chitin obtained via pyrolysis at mild conditions. Appl Surf Sci 427:883–893

11. Parsimehr H, Ehsani A (2020) Algae-based electrochemical energy storage devices. Green Chem 22(23):8062–8096

12. Thines KR, Abdullah EC, Mubarak NM, Ruthiraan M (2017) In-situ polymerization of magnetic biochar – polypyrrole composite: a novel application in supercapacitor. Biomass Bioenergy 98:95–111

13. Rout T, Pradhan D, Singh RK, Kumari N (2016) Exhaustive study of products obtained from coconut shell pyrolysis. J Environ Chem Eng 4(3):3696–3705

14. Zhu L, Lei H, Wang L, Yadavalli G, Zhang X, Wei Y, Liu Y, Yan D, Chen S, Ahring B (2015) Biochar of corn stover: Microwave-assisted pyrolysis condition induced changes in surface functional groups and characteristics. J Anal Appl Pyrolysis 115:149–156

15. Kizito S, Wu S, Kipkemoi Kirui W, Lei M, Lu Q, Bah H, Dong R (2015) Evaluation of slow pyrolyzed wood and rice husks biochar for adsorption of ammonium nitrogen from piggery manure anaerobic digestate slurry. Sci Total Environ 505:102–112

16. Agrafioti E, Kalderis D, Diamadopoulos E (2014) Arsenic and chromium removal from water using biochars derived from rice husk, organic solid wastes and sewage sludge. J Environ Manag 133:309–314

17. Demirbas A (2004) Effects of temperature and particle size on biochar yield from pyrolysis of agricultural residues. J Anal Appl Pyrolysis 72(2):243–248

18. Shabangu S, Woolf D, Fisher EM, Angenent LT, Lehmann J (2014) Techno-economic assessment of biomass slow pyrolysis into different biochar and methanol concepts. Fuel 117:742–748

19. Budai A, Wang L, Gronli M, Strand LT, Antal MJ, Abiven S, Dieguez-Alonso A, Anca-Couce A, Rasse DP (2014) Surface properties and chemical composition of corncob and Miscanthus biochars: effects of production temperature and method. J Agric Food Chem 62(17):3791–3799

20. Sánchez ME, Menéndez JA, Domínguez A, Pis JJ, Martínez O, Calvo LF, Bernad PL (2009) Effect of pyrolysis temperature on the composition of the oils obtained from sewage sludge. Biomass Bioenergy 33(6):933–940

21. Salema AA, Afzal MT, Bennamoun L (2017) Pyrolysis of corn stalk biomass briquettes in a scaled-up microwave technology. Bioresour Technol 233:353–362

22. Cazetta AL, Pezoti O, Bedin KC, Silva TL, Paesano Junior A, Asefa T, Almeida VC (2016) Magnetic activated carbon derived from biomass waste by concurrent synthesis: efficient adsorbent for toxic dyes. ACS Sustain Chem Eng 4(3):1058–1068

23. Zhou N, Chen H, Xi J, Yao D, Zhou Z, Tian Y, Lu X (2017) Biochars with excellent Pb(II) adsorption property produced from fresh and dehydrated banana peels via hydrothermal carbonization. Bioresour Technol 232:204–210

24. Lam SS, Chase HA (2012) A review on waste to energy processes using microwave pyrolysis. Energies 5(10):4209–4232

25. Cao X, Sun S, Sun R (2017) Application of biochar-based catalysts in biomass upgrading: a review. RSC Adv 7(77):48793–48805

26. Cheng B-H, Zeng RJ, Jiang H (2017) Recent developments of post-modification of biochar for electrochemical energy storage. Bioresour Technol 246:224–233

27. Xiu S, Shahbazi A, Li R (2017) Characterization, Modification and application of biochar for energy storage and catalysis: a review. Trends in Renewable Energy 3(1):86–101

28. Kambo HS, Dutta A (2015) A comparative review of biochar and hydrochar in terms of production, physico-chemical properties and applications. Renew Sust Energ Rev 45:359–378

29. Angın D, Altintig E, Köse TE (2013) Influence of process parameters on the surface and chemical properties of activated carbon obtained from biochar by chemical activation. Bioresour Technol 148:542–549

30. Thomas D, Fernandez NB, Mullassery MD, Surya R (2020) Iron oxide loaded biochar/polyaniline nanocomposite: synthesis, characterization and electrochemical analysis. Inorg Chem Commun 119:108097

31. Wang P, Zhang G, Li M-Y, Yin Y-X, Li J-Y, Li G, Wang W-P, Peng W, Cao F-F, Guo Y-G (2019) Porous carbon for high-energy density symmetrical supercapacitor and lithium-ion hybrid electrochemical capacitors. Chem Eng J 375:122020

32. Thines KR, Abdullah EC, Mubarak NM (2017) Effect of process parameters for production of microporous magnetic biochar derived from agriculture waste biomass. Microporous Mesoporous Mater 253:29–39

33. Sun Y, Gao B, Yao Y, Fang J, Zhang M, Zhou Y, Chen H, Yang L (2014) Effects of feedstock type, production method, and pyrolysis temperature on biochar and hydrochar properties. Chem Eng J 240:574–578

34. Park JH, Ok YS, Kim SH, Cho JS, Heo JS, Delaune RD, Seo DC (2015) Evaluation of phosphorus adsorption capacity of sesame straw biochar on aqueous solution: influence of activation methods and pyrolysis temperatures. Environ Geochem Health 37(6):969–983

35. Sarswat A, Mohan D (2016) Sustainable development of coconut shell activated carbon (CSAC) and a magnetic coconut shell activated carbon (MCSAC) for phenol (2-nitrophenol) removal. RSC Adv 6(88):85390–85410

36. M. Azmier, N. Ahmad, O. Bello, Modified durian seed as adsorbent for the removal of methyl red dye from aqueous solutions, Applied Water Science 5 (2014).

37. Enaime G, Baçaoui A, Yaacoubi A, Lübken M (2020) Biochar for wastewater treatment—conversion technologies and applications. Appl Sci 10(10):3492

38. Wang H, Gao B, Wang S, Fang J, Xue Y, Yang K (2015) Removal of Pb(II), Cu(II), and Cd(II) from aqueous solutions by biochar derived from KMnO4 treated hickory wood. Bioresour Technol 197:356–362

39. Sarkar JK, Wang Q (2020) Different pyrolysis process conditions of South Asian waste coconut shell and characterization of gas, bio-char, and bio-oil. Energies 13(8):1970

40. Liu H, Xu F, Xie Y, Wang C, Zhang A, Li L, Xu H (2018) Effect of modified coconut shell biochar on availability of heavy metals and biochemical characteristics of soil in multiple heavy metals contaminated soil. Sci Total Environ 645:702–709

41. Yan Z, Song N, Cai H, Tay J-H, Jiang H (2012) Enhanced degradation of phenanthrene and pyrene in freshwater sediments by combined employment of sediment microbial fuel cell and amorphous ferric hydroxide. J Hazard Mater 199-200:217–225

42. Zhang L, Tu L-y, Liang Y, Chen Q, Li Z-s, Li C-h, Wang Z-h, Li W (2018) Coconut-based activated carbon fibers for efficient adsorption of various organic dyes. RSC Adv 8(74):42280–42291

43. Hao Z, Wang C, Yan Z, Jiang H, Xu H (2018) Magnetic particles modification of coconut shell-derived activated carbon and biochar for effective removal of phenol from water. Chemosphere 211:962–969

44. Üner O, Geçgel Ü, Bayrak Y (2015) Preparation and characterization of mesoporous activated carbons from waste watermelon rind by using the chemical activation method with zinc chloride. Arab J Chem

45. Thines KR, Abdullah EC, Ruthiraan M, Mubarak NM, Tripathi M (2016) A new route of magnetic biochar based polyaniline composites for supercapacitor electrode materials. J Anal Appl Pyrolysis 121:240–257

46. Zhao Y, Zhang R, Liu H, Li M, Chen T, Chen D, Zou X, Frost RL (2019) Green preparation of magnetic biochar for the effective accumulation of Pb(II): performance and mechanism. Chem Eng J 375:122011

47. Mo R-J, Zhao Y, Wu M, Xiao H-M, Kuga S, Huang Y, Li J-P, Fu S-Y (2016) Activated carbon from nitrogen rich watermelon rind for high-performance supercapacitors. RSC Adv 6(64):59333–59342

48. Saleh S, Kamarudin KB, Ghani WAWAK, Kheang LS (2016) Removal of organic contaminant from aqueous solution using magnetic biochar. Procedia Eng 148:228–235

49. Oh W-D, Lua S-K, Dong Z, Lim T-T (2015) Performance of magnetic activated carbon composite as peroxymonosulfate activator and regenerable adsorbent via sulfate radical-mediated oxidation processes. J Hazard Mater 284:1–9

50. D. Das, D. Samal, M. Bc, Preparation of activated carbon from green coconut shell and its characterization, Journal of Chemical Engineering & Process Technology 06 (2015).

51. Sharma RK, Chan WG, Hajaligol MR (2009) Effect of reaction conditions on product distribution from the co-pyrolysis of α-amino acids with glucose. J Anal Appl Pyrolysis 86(1):122–134

52. Lee XJ, Lee LY, Gan S, Thangalazhy-Gopakumar S, Ng HK (2017) Biochar potential evaluation of palm oil wastes through slow pyrolysis: Thermochemical characterization and pyrolytic kinetic studies. Bioresour Technol 236:155–163

53. N. Lan Huong, T. Nguyen, H.T. Van, V. Xuan Hoa, T. Ha, T. Nguyen, X. Nguyen, N. Ca, Treatment of hexavalent chromium contaminated wastewater using activated carbon derived from coconut shell loaded by silver nanoparticles: batch experiment, Water, Air, & Soil Pollution 230 (2019).

54. Li H, Xiong J, Xiao T, Long J, Wang Q, Li K, Liu X, Zhang G, Zhang H (2019) Biochar derived from watermelon rinds as regenerable adsorbent for efficient removal of thallium(I) from wastewater. Process Saf Environ Prot 127:257–266

55. Fu P, Yi W, Bai X, Li Z, Hu S, Xiang J (2011) Effect of temperature on gas composition and char structural features of pyrolyzed agricultural residues. Bioresour Technol 102(17):8211–8219

56. Zhang M, Gao B, Varnoosfaderani S, Hebard A, Yao Y, Inyang M (2013) Preparation and characterization of a novel magnetic biochar for arsenic removal. Bioresour Technol 130:457–462

57. Kante K, Deliyanni E, Bandosz TJ (2009) Interactions of NO2 with activated carbons modified with cerium, lanthanum and sodium chlorides. J Hazard Mater 165(1):704–713

58. Machala L, Tuček J, Zbořil R (2011) Polymorphous transformations of nanometric iron(III) oxide: a review. Chem Mater 23(14): 3255–3272

59. E. Taer, A. Agustino, R. Farma, R. Taslim, Awitdrus, M. Paiszal, A. Ira, S.D. Yardi, Y.P. Sari, H. Yusra, S. Nurjanah, S.D. Hartati, Z. Aini, R.N. Setiadi, The relationship of surface area to cell capacitance for monolith carbon electrode from biomass materials for supercapacitor aplication, Journal of Physics: Conference Series 1116 (2018) 032040.

60. Muzaffar A, Ahamed MB, Deshmukh K, Thirumalai J (2019) A review on recent advances in hybrid supercapacitors: design, fabrication and applications. Renew Sust Energ Rev 101:123–145

61. T. Abbas, N. Akter, M.S. Alam, D.S. Alessi, A. Ali, S. Ali, M.S. Azam, A. Bashir, L. Beesley, N. Bolan, Z. Cai, L. Cui, C.E. Egene, A. El-Naggar, S.Y. Gladys Choo, S.R. Gunatilake, K. Hall, N.E.E. Hassan, B. Hudcová, J.A. Ippolito, S.-H. Jien, M.G. Johnson, M. Komárek, H.W. Kua, E.E. Kwon, J. Lee, Q. Li, X. Li, B. Liu, G. Liu, S.-H. Liu, J. Luo, A. Maqbool, E. Moore, N.K. Niazi, J.M. Novak, N.L. Obadamudalige, Y.S. Ok, C. Peiris, M.Z.u. Rehman, J. Rinklebe, M. Rizwan, A.K. Sarmah, S.M. Shaheen, H. Shang, K.A. Spokas, F.M.G. Tack, R. Tareq, L. Trakal, D.C.W. Tsang, M. Vithanage, M. Vítková, H. Wang, J. Wang, X. Wang, J.J. Wewalwela, A. Williams, X. Xiong, Y. Xu, Y. Yan, X. Yang, S. You, I.K.M. Yu, C. Zhang, M. Zhang, S. Zhang, W. Zhang, C. Zhao, H. Zheng, S. Zhou, X. Zhu, List of Contributors, in: Y.S. Ok, D.C.W. Tsang, N. Bolan, J.M. Novak (Eds.), Biochar from Biomass and Waste, Elsevier2019, pp. xi-xv.